Strain and Band-Gap Engineering in Ge-Sn Alloys via P Doping

Slawomir Prucnal,[1,*] Yonder Berencén,[1] Mao Wang,[1] Jörg Grenzer,[1] Matthias Voelskow,[1] Rene Hübner,[1] Yuji Yamamoto,[3] Alexander Scheit,[3] Florian Bärwolf,[3] Vitaly Zviagin,[5] Rüdiger Schmidt-Grund,[5] Marius Grundmann,[5] Jerzy Żuk,[2] Marcin Turek,[2] Andrzej Droździel,[2] Krzysztof Pyszniak,[2] Robert Kudrawiec,[6] Maciej P. Polak,[6] Lars Rebohle,[1] Wolfgang Skorupa,[1] Manfred Helm,[1,4] and Shengqiang Zhou[1]

[1] *Institute of Ion Beam Physics and Materials Research, Helmholtz-Zentrum Dresden-Rossendorf, P.O. Box 510119, 01314 Dresden, Germany*

[2] *Maria Curie-Skłodowska University, Plac M. Curie-Skłodowskiej 1, 20-035 Lublin, Poland*

[3] *IHP, Im Technologiepark 25, 15236 Frankfurt (Oder), Germany*

[4] *Center for Advancing Electronics Dresden, Technische Universität Dresden, 01062 Dresden, Germany*

[5] *Felix-Bloch-Institut für Festkörperphysik, Universität Leipzig, Linnéstraße 5, 04103 Leipzig, Germany*

[6] *Faculty of Fundamental Problems of Technology, Wroclaw University of Science and Technology, Wybrzeże Wyspiańskiego 27, 50-370 Wrocław, Poland*

(Received 6 July 2018; revised manuscript received 11 October 2018; published 21 December 2018)

Ge with a quasi-direct band gap can be realized by strain engineering, alloying with Sn, or ultrahigh *n*-type doping. In this work, we use all three approaches together to fabricate direct-band-gap Ge-Sn alloys. The heavily doped *n*-type Ge-Sn is realized with CMOS-compatible nonequilibrium material processing. P is used to form highly doped *n*-type Ge-Sn layers and to modify the lattice parameter of P-doped Ge-Sn alloys. The strain engineering in heavily-P-doped Ge-Sn films is confirmed by x-ray diffraction and micro Raman spectroscopy. The change of the band gap in P-doped Ge-Sn alloy as a function of P concentration is theoretically predicted by density functional theory and experimentally verified by near-infrared spectroscopic ellipsometry. According to the shift of the absorption edge, it is shown that for an electron concentration greater than 1×10^{20} cm^{-3} the band-gap renormalization is partially compensated by the Burstein-Moss effect. These results indicate that Ge-based materials have high potential for use in near-infrared optoelectronic devices, fully compatible with CMOS technology.

DOI: 10.1103/PhysRevApplied.10.064055

I. INTRODUCTION

Ge, with much higher electron and hole mobilities than in Si, is one of the most promising materials that can boost the performance of nanoelectronic devices even further. Because of its chemical and physical similarity to Si, Ge can be integrated into CMOS technology. Intrinsic bulk Ge is an indirect-band-gap material, but it can be converted to a quasi-direct band gap material due to the small separation between the Γ valley and the L valley (136 meV) [1]. It was shown that the direct band gap of Ge can be realized by tensile-strain engineering, alloying with Sn, or ultrahigh *n*-type doping [2–5]. With use of only one of these methods it is extremely difficult to achieve a direct band gap. The biaxial tensile strain required for the direct-band-gap formation in Ge has to be greater than 1.9% [6]. One achieves this by growing Ge on foreign substrates with a lattice parameter much larger than that of Ge; for example, on (In,Ga)As [7]. Unfortunately, this approach requires the use of GaAs substrates and processes that are not compatible with CMOS technology.

Kimerling's group [5] has grown relaxed Ge on a Si substrate using high-temperature annealing and fast cooling. Because of the different expansion coefficients of Si and Ge, the layer created has a tensile strain of 0.25%. The predicted maximal biaxial tensile strain that can be obtained by this method (0.35%) is far below the required 1.9% to form a direct band gap in Ge. Nevertheless, the remaining difference between the Γ valley and the L valley (115 meV) can be compensated by *n*-type doping. The minimum electron concentration needed to completely fill the L valley and to start the population of the Γ valley is on the order of 8×10^{19} cm^{-3}. The main advantage of this method is that the main optical emission under such conditions is at about 1550 nm [5], which matches perfectly with the optical window of quartz fibers, but attaining such a doping level remains challenging.

Recently, much more effort has been devoted to the fabrication of direct-band-gap Ge-Sn alloys. It was shown that Ge-Sn with a Sn concentration higher than 8% can be

*s.prucnal@hzdr.de

 © 2018 American Physical Society

TABLE I. Ion-implantation parameters together with electron concentration and electron mobility obtained by Hall-effect measurements at 2.5 and 300 K, respectively.

Sample	Sn fluence at 250 keV (cm^{-2})	P fluence at 80 keV (cm^{-2})	Carrier concentration (cm^{-3}) 2.5 K	Carrier concentration (cm^{-3}) 300 K	Carrier mobility at 300 K (cm^2/V s)
GeP2	⋯	6.0×10^{15}	9.1×10^{19}	9.6×10^{19}	162
Ge-Sn	1.0×10^{16}	⋯			
GeSnP1	1.0×10^{16}	3.0×10^{15}	7.0×10^{19}	7.2×10^{19}	140
GeSnP2	1.0×10^{16}	6.0×10^{15}	8.5×10^{19}	8.8×10^{19}	164
GeSnP3	1.0×10^{16}	9.0×10^{15}	9.5×10^{19}	10.5×10^{19}	175

converted to a direct-band-gap semiconductor that shows optically driven lasing at low temperatures [8,9]. The compressive strain formed in Ge-Sn due to the lattice mismatch between Ge-Sn and Ge increases the direct gap, which in turn requires even higher concentrations of Sn to achieve a direct gap.

In this paper, we report on a combined approach toward direct-band-gap Ge-Sn by codoping with P that in turn not only compensates the biaxial compressive strain in Ge-Sn but also introduces ultrahigh *n*-type doping. The ultradoped *n*-type Ge-Sn layer on Si is fabricated by ion implantation of Sn and P into Ge-on-Si wafers followed by nonequilibrium millisecond-range rear-side flash-lamp annealing (RFLA). Recrystallization of the ion-implanted layer and the electrical activation of P are induced by explosive-solid-phase-epitaxy (ESPE) regrowth [10,11]. According to x-ray-diffraction (XRD) data, the lattice parameter of P-doped $Ge_{0.97}Sn_{0.03}$ alloy in comparison with the relaxed $Ge_{0.97}Sn_{0.03}$ binary alloy is reduced by 0.42% ($a_{Ge0.97Sn0.03:P} = 5.659$ Å vs $a_{Ge0.97Sn0.03} = 5.683$ Å). The band-gap change of the fabricated P-doped $Ge_{0.97}Sn_{0.03}$ alloys cannot be explained just by either the alloy formation or the band-gap renormalization. The influence of the reduction of the lattice parameter on the band-gap change together with the Burstein-Moss effect has to be considered. The fabricated P-doped Ge-Sn alloys are of *n* type with an electron concentration as high as 1×10^{20} cm^{-3}.

II. EXPERIMENTAL SECTION

A 475-nm-thick undoped Ge layer is epitaxially grown on a Si(100) substrate by reduced-pressure chemical vapor deposition at IHP Frankfurt (Oder). Before ion implantation, a 30-nm-thick SiO_2 layer is deposited by plasma-enhanced chemical vapor deposition. SiO_2 is used to prevent the Ge surface from roughening and sputtering during ion implantation [12,13]. Subsequently, Sn and P are implanted in the samples (see Table I for details). After ion implantation, an ultrashort nonequilibrium thermal processing is applied. Before this step, samples are preheated to 180 °C for 30 s in a nitrogen ambient atmosphere. Samples are subsequently subjected to RFLA for 3 ms at an energy density of 61.5 J cm^{-2} deposited onto the rear side of the sample. The RFLA process is described in detail elsewhere [10]. In recent years, flash-lamp annealing (FLA) has been used as an annealing method in the millisecond range for many purposes, especially driven by the needs of advanced semiconductor processing (see Refs. [14–16] for recent reviews) and, more specifically, also those of Ge-based materials research: shallow junctions [17], nanoclusters [18], advanced processing [10,19], etc.

The incorporation efficiency of Sn into Ge during explosive recrystallization is investigated by random Rutherford backscattering spectrometry (RBS/R) and channeling Rutherford backscattering spectrometry (RBS/C). RBS is performed with the 1.7-MeV He^+ beam of the Rossendorf van de Graff accelerator. P and Sn concentrations versus depth profiles are measured by a dynamic secondary-ion mass spectrometer (SIMS) with 1-keV Cs^+ and O^+ sputter beams, respectively. Beams of Cs^+ or O^+ ions are rastered over a surface area of 300×300 μm^2 and secondary ions are collected from the central part of the sputtered crater. Crater depths are measured with a Dektak 8 stylus profilometer, and a constant erosion rate is assumed for conversion of the sputtering time to the sample depth.

To investigate the microstructural properties of the ion-implanted Ge layer, cross-section bright-field and high-resolution transmission electron-microscopy (TEM) are performed with a Titan 80-300 (FEI) microscope operated at an accelerating voltage of 300 kV. High-angle-annular-dark-field (HAADF) scanning-transmission-electron-microscopy (STEM) imaging and element mapping based on energy-dispersive x-ray spectroscopy (EDXS) are performed at 200 kV with a Talos F200X microscope equipped with a Super-X EDXS detector system (FEI). Before TEM analysis, the specimen mounted in a high-visibility low-background holder is placed for 10 s into a model 1020 plasma cleaner (Fischione) to remove contamination.

The strain evolution in both the ion-implanted and the annealed samples is investigated by micro Raman spectroscopy and XRD. XRD is performed with a

Panalytical Empyrean diffractometer with a Cu-target source. The setup is equipped with a Göbel mirror and an asymmetric monochromator to enhance the brilliance and monochromaticity.

The band-gap change in (Ge,Sn)P ternary alloys is determined by means of spectroscopic ellipsometry. The thin-film complex dielectric function is obtained by variable-angle spectroscopic ellipsometry in a polarizer-compensator-sample-analyzer configuration from J.A. Woolam. Measurements are conducted at room temperature in the spectral range from 0.5 to 4.0 eV. The ellipsometry spectra are analyzed by a model consisting of a layer stack as follows: (from the bottom) the substrate, the Ge-Sn and (Ge,Sn)P film layer, and a surface layer with a 50% mix of the dielectric function of the topmost film and air. The optical constants of the modified thin layers are determined numerically by use of a Kramers-Kronig consistent B-spline approximation with a knot-number-choice approach described elsewhere [20]. The optical layer thickness shows general agreement with the RBS and SIMS measurements. The fit obtained agrees well with the experimental data with a mean square error of less than 2.2. The reflected light is detected by a Si diode and an (In,Ga)As diode in the ultraviolet-visible spectral range and the near-infrared spectral range, respectively.

The concentration of carriers in the ion-implanted and annealed samples is estimated from temperature-dependent Hall-effect measurements in a van der Pauw configuration. The thickness of the doped layer is extracted from SIMS measurements.

The band structure and position of the Fermi energy in P-doped Ge-Sn alloys are calculated with the full-potential linearized-augmented-plane-wave (FPLAPW) WIEN2k code in a supercell approach with the modified Becke-Johnson local-density approximation (MBJLDA) and the spectral-weight approach used for the band-gap correction and for band unfolding, respectively.

III. RESULTS AND DISCUSSION

A. Microstructural properties

The redistribution of the implanted elements and their lattice location in the Ge film are investigated by RBS performed in random and channeling directions on both as-implanted samples and annealed samples [see Fig. 1(a)]. The RBS random spectrum obtained from GeSnP2 exhibits three distinct regions, corresponding to Si with detection energies below 690 keV (the Si signal from the substrate), Ge registered in the energy range from 1030 and 1380 keV (475-nm-thick Ge on the Si substrate), and Sn observed between 1400 and 1500 keV. In the as-implanted stage, the RBS/C spectrum can be used to calculate the concentration of Sn in Ge and to estimate the thickness of the ion-implanted region. Unfortunately, P is not resolvable in our RBS spectra because P is much lighter than the matrix elements and its signal overlaps with the Ge signal. The thickness of the ion-implanted layer can be calculated from the Ge signal in the RBS/C spectrum. Because of the end-of-range defects and the large implantation fluence of P, the total thickness of the almost-amorphous Ge layer formed during ion implantation is 230 nm, compared with the assumed thickness of 200 nm of the P-doped layer as calculated by SRIM [21]. Considering the three P fluences and the thickness of the ion-implanted layer, the deduced P peak concentrations are 1.5×10^{20} cm^{-3} (GeSnP1), 3.0×10^{20} cm^{-3} (GeSnP2), and 4.5×10^{20} cm^{-3} (GeSnP3). The Sn-doped

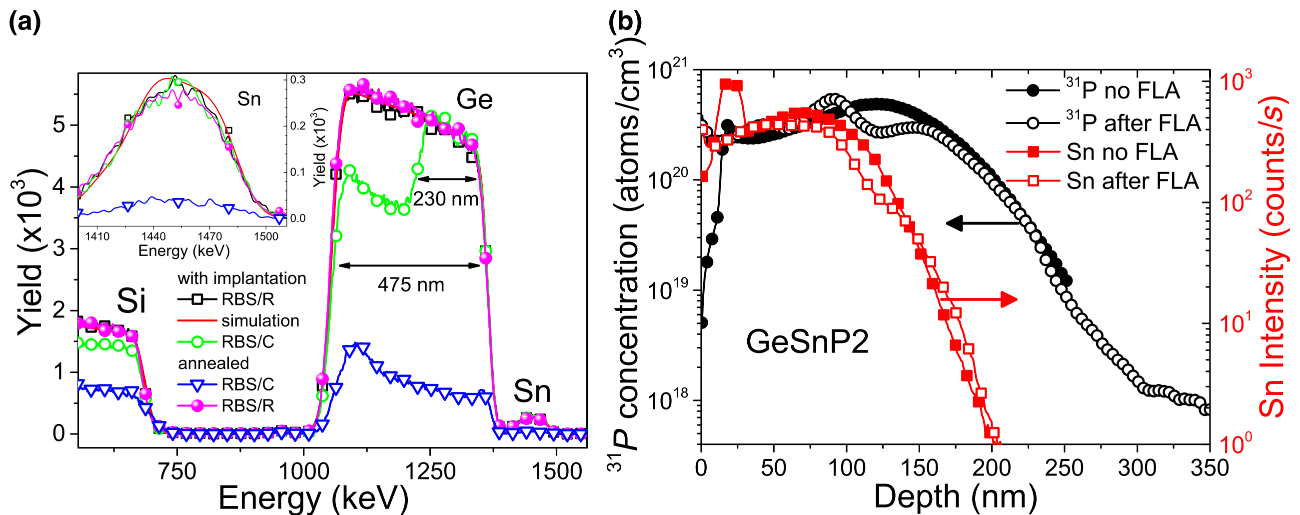

FIG. 1. (a) RBS random and channeling spectra obtained from the as-implanted and annealed GeSnP2 samples. The inset shows magnified Sn-related RBS spectra. (b) P and Sn distribution in the Ge layer before and after FLA obtained by SIMS measurements. FLA was performed for 3 ms at an energy density of 61.5 J cm^{-2}.

layer is about 150 nm thick, and the Sn peak concentration calculated from the RBS/R spectrum is 3.0% in all the samples investigated. According to the RBS/R and SIMS measurements, the distribution of Sn in the annealed samples remains unchanged compared with the as-implanted sample, confirming that there is no remarkable diffusion of Sn during millisecond-range FLA [see the inset in Fig. 1(a) and Fig. 1(b)].

The RBS/C investigation performed on the annealed samples provides information about the recrystallization efficiency of the ion-implanted layer and the lattice location of the implanted elements. In the ideal crystal, close to the surface region (the first 100 nm), the yield of the RBS/C spectrum should be less than 10% of that obtained under random conditions. In the FLA-treated sample, the RBS/C signal from Sn is hardly visible, which means that Sn is fully incorporated into the Ge lattice. The Sn content in the fabricated P-doped Ge-Sn alloy is more than 5 times greater than the equilibrium solid solubility limit of Sn in Ge.

Moreover, according to the RBS results, the quality of the P-doped Ge-Sn alloy is independent of the P fluence within the range investigated. The yield of the Ge signal in RBS/C is also low, confirming a high recrystallization efficiency during FLA. Since P atoms could not be resolved by RBS, SIMS is used as an alternative method to observe the depth distribution of P in Ge before and after FLA. Figure 1(b) shows the distribution of P (left axis) and Sn (right axis) in GeSnP2. The Ge layer containing Sn is homogenously doped with P and has a thickness of about 150 nm, while the total thickness of the *n*-type layer is 220 nm. The Sn distribution with an atomic concentration far exceeding the equilibrium solubility limit in Ge does not show a significant difference between the as-implanted stage and the flash-lamp-annealed one. A similar phenomenon is observed for P. The small variation in the P concentration between 100 and 170 nm can be caused by P being trapped at the interface between Ge-Sn and Ge. Nevertheless, the maximum P concentration and the depth distribution are almost unaffected by FLA. This confirms the RBS results as well as our assumption about the use of millisecond-range FLA for the realization of a highly-P-doped *n*-type Ge-Sn layer with a well-controlled doping profile. With use of RFLA, the ion-implanted layer recrystallizes via ESPE. During ESPE the amorphous/crystalline interface moves toward the surface with a speed of about 10 m/s, which is much faster than the diffusion of most dopants in Ge in the solid state [22]. Phenomena such as the snowplow effect are not observed in our annealed films [23,24].

Figures 2(a) and 2(b) show cross-section bright-field- and high-resolution-TEM images, respectively, obtained from GeSnP2 after FLA for 3 ms. Within the area investigated, the single-crystal structure is restored, and even the end-of-range defects typical of ion-implanted semiconductors is not visible [25]. Only threading dislocations are detected at the interface between bulk Si and the grown Ge layer. The presence of such defects is typical for binary systems epitaxially grown with different lattice parameters [26]. In our case, the lattice mismatch between Ge and Si is on the order of 4% and the threading dislocations annihilate completely within the first 200 nm of the grown layer. Figures 2(d)–2(f) present the element distributions of Ge, Sn, and Si based on EDXS-spectrum imaging in STEM mode from the window marked by the white rectangle in the HAADF-STEM image in Fig. 2(c). As can be seen in Figs. 2(e) and 2(f), Sn is evenly distributed in Ge over the implantation depth. No clusters or agglomerates of Sn are detected, which is in good agreement with SIMS and RBS data.

B. Strain engineering

1. X-ray diffraction

To obtain the in-plane and out-of-plane strain distribution in the fabricated Ge-Sn films XRD θ-2θ scans are performed and reciprocal-space maps are obtained (see Fig. 3). The in-plane lattice parameter of the Ge virtual substrate is $a = 5.659$ Å, while the out-of-plane lattice parameter is $b = 5.642$ Å. This means that already the as-deposited Ge layer is slightly biaxially tensile strained ($\epsilon = 0.16\%$).

The biaxial tensile strain obtained from XRD measurements is in good agreement with Raman data (see Fig. 4). The FLA performed on the as-deposited sample has no influence on the strain distribution, but the reciprocal-space map suggests an improvement of the crystal quality due to the annealing of some defects (e.g., threading dislocations). The high-resolution-XRD θ-2θ scan around Ge(004) reveals no significant changes in the Ge virtual substrate due to ion implantation followed by nonequilibrium FLA. After Sn implantation and annealing, the additional peak at lower scattering angles describes the lattice expansion along [001]. The shift is caused by the formation of Ge-Sn. Because the lattice parameter of relaxed Ge-Sn is bigger than that of the Ge virtual substrate, the fabricated Ge-Sn alloy is biaxially compressively strained. The XRD θ-2θ scan performed along (004) and reciprocal-space maps show that the biaxial compressive strain in Ge-Sn can be effectively compensated by codoping with P. The in-plane lattice parameter a is the same in both the Ge virtual substrate and the fabricated Ge-Sn layer ($a = 5.659$ Å), while the out-of-plane lattice parameter b in Ge-Sn alloys decreases from 5.671 Å in GeSnP1 to 5.659 Å in GeSnP3.

The lattice parameters for different samples are summarized in Table II. Sn has a bigger covalent radius than Ge (140 pm vs 120 pm, about 16% difference), which is why the lattice parameter of the relaxed Ge-Sn alloy should be bigger than that of undoped Ge. The covalent radius of

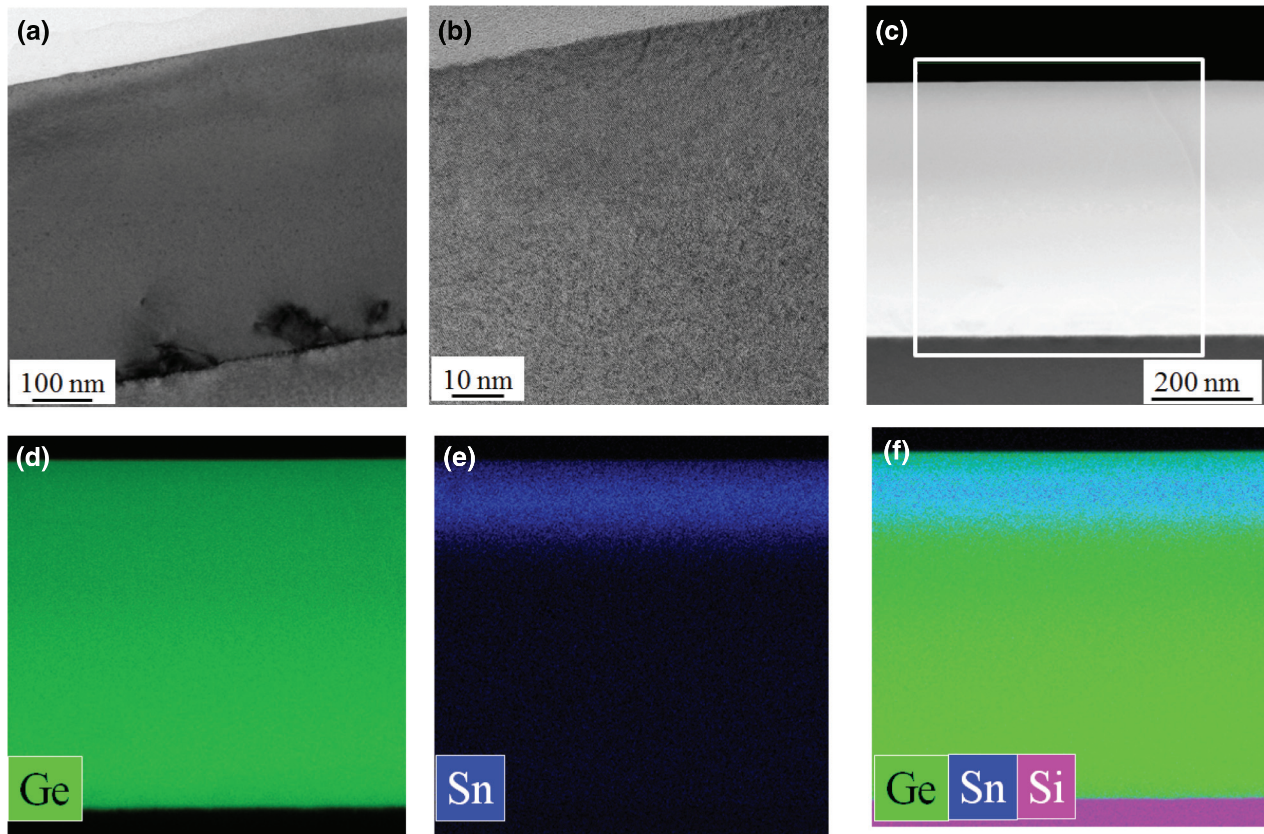

FIG. 2. (a) Cross-section bright-field-TEM micrograph and (b) high-resolution-TEM image of Ge into which Sn and P ions are implanted after FLA for 3 ms. (c) Cross-section HAADF-STEM image and (d) Ge (green) distribution, (e) Sn (blue) distribution, and (f) superimposed Si, Ge, and Sn element distributions based on EDXS obtained in STEM mode for the region marked by the white rectangle in (c).

P (107 pm) is about 11% smaller than that of Ge. This means that P can efficiently reduce the lattice parameter of P-doped Ge-Sn and compensates the biaxial compressive strain. Even the electronic contribution, which normally expands the lattice, cannot compensate the effect of P doping [28]. According to the theoretical prediction, the lattice contraction in Ge doped with P at a concentration of 1.2×10^{20} cm^{-3} is on the order of 2% [28]. In our case, the highest P concentration in the Ge-Sn layer is close to 5×10^{20} cm^{-3}, indicating a significant lattice contraction (close to 4%) if P lies in the substitutional position. Simultaneously, the biaxial tensile strain in the Ge virtual substrate remains. If the Ge virtual substrate is replaced by a substrate with a bigger lattice parameter (e.g., Ge-Sn with 3% Sn), a tensile-strained ultradoped Ge-Sn layer can even be formed, favoring the formation of a direct band gap.

2. Micro Raman spectroscopy

Figure 4 shows the micro Raman spectra obtained from an as-deposited Ge-on-Si sample, a nonimplanted but annealed sample, and samples in which both Sn and P are implanted followed by millisecond-range RFLA. Because of the limited penetration depth of the green laser light in Ge and Ge-Sn, the Raman spectra presented contain only the signal from the top 50 nm of the layer. The main peak observed from the as-deposited film corresponds to the transverse optical (TO) phonon mode in Ge, which is located at 299.9 ± 0.1 cm^{-1}. In undoped and fully relaxed Ge, the TO phonon mode should be located at 300.5 cm^{-1}. The shift of the TO phonon mode toward smaller wavenumbers can be explained in terms of tensile strain.

The lattice parameter of Si is 4.2% smaller than that of Ge, and thus it is expected that the Ge layer grown on Si should be compressively strained. However, because of the different thermal expansion coefficients of Ge and Si, the Ge layer is tensile strained after the postgrown thermal treatment [29]. Moreover, the alloying of Ge with heavier elements such as Sn or Pb shifts the position of the TO phonon mode toward smaller wavenumbers, while alloying with lighter elements such as Si shifts the TO phonon mode toward larger wavenumbers.

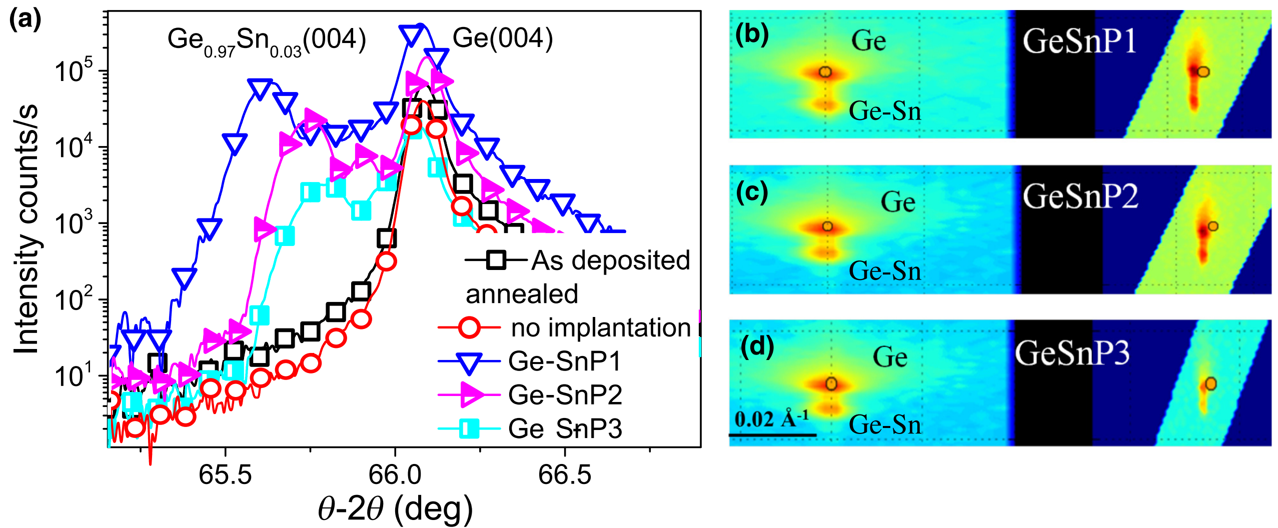

FIG. 3. XRD θ-2θ scans around the Ge(004) diffraction of ion-implanted and FLA-treated samples, the virgin Ge-on-Si wafer, and the annealed sample without implantation (a) (curves are shifted vertically for clarity). (b)– (d) Reciprocal-space maps around the (004) (left panels) and (224) (right panels) reflections of Ge and Ge-Sn after ion implantation and FLA. The orange circles in the reciprocal-space maps describe the expected theoretical positions of a fully relaxed pseudomorphic Ge lattice.

Taking the shift of $\Delta\omega = -0.6 \pm 1$ cm^{-1} into account, we can calculate the strain using the following expression [30]:

$$\varepsilon = \left(\frac{\Delta\omega}{c}\right) \times 100\%, \tag{1}$$

where $\Delta\omega$ is the shift of the phonon-mode position and c is a prefactor (approximately -300 for Ge). Positive ϵ corresponds to tensile strain, while negative ϵ describes compressive strain. According to the peak position of the TO phonon mode in the Raman spectrum, the as-grown Ge layer exhibits a tensile strain of $(0.20 \pm 0.03)\%$, which is in good agreement with the value calculated from XRD data ($\epsilon = 0.16\%$). The RFLA performed on the nonimplanted sample does not affect the strain redistribution in the Ge layer.

In the case of relaxed Ge-Sn alloy, the Raman-peak shift of the Ge—Ge LO mode is caused by the mass disorder (Ge vs much heavier Sn) and the bond distortion (Ge—Ge bond vs much longer Ge—Sn bond). Assuming a fully relaxed Ge-Sn film with 3% Sn, the shift of the peak position of the TO phonon mode in the Raman spectrum in Ge-Sn film ($\Delta\omega$) [30] can be calculated according to

$$\Delta\omega = \omega_{\text{Ge - Sn}} - \omega_{\text{Ge}} = c \times x_{\text{Sn}}, \tag{2}$$

where $\omega_{\text{Ge-Sn}}$ and ω_{Ge} are the TO phonon modes in relaxed Ge-Sn alloy and intrinsic Ge, x_{Sn} is the Sn concentration in Ge-Sn alloy, and $c = -82.8$ after Ref. [30]. Because of

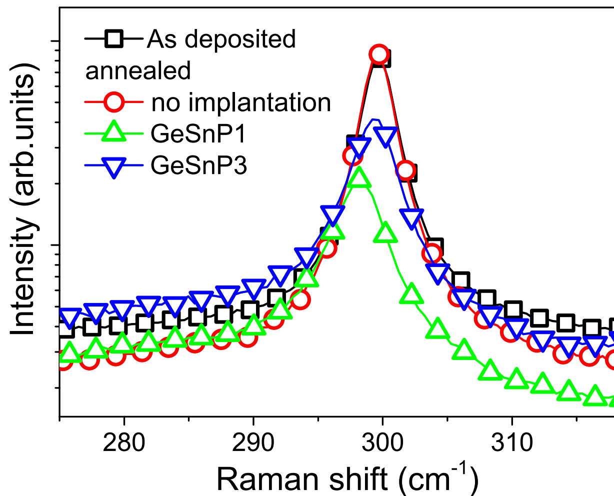

FIG. 4. Micro Raman spectra obtained from as-deposited and ion-implanted Ge-on-Si wafers after RFLA.

TABLE II. In-plane and out-of-plane lattice parameters of implanted and annealed samples. The calculated lattice parameters for relaxed $Ge_{0.97}Sn_{0.03}$ are also given.

Sample	In-plane a (Å)	Out-of-plane b (Å)
Ge pseudosubstrate	5.659	5.642
GeSnP1	5.659	5.671
GeSnP2	5.659	5.665
GeSnP3	5.659	5.659
$Ge_{0.97}Sn_{0.03}$	5.683[a]	5.683[a]

[a] $a_{\text{Ge-Sn}}$ in relaxed $Ge_{0.97}Sn_{0.03}$ is calculated with the following expression: $a_0 = a_{\text{Sn}} \times x + a_{\text{Ge}}(1-x) + bx(1-x)$, where $a_{\text{Sn}} = 6.4892$ Å, $a_{\text{Ge}} = 5.6579$ Å, $b = 0.00882$ Å, and $x = 0.03$ [27].

the lattice mismatch (between the Ge virtual substrate and Ge-Sn alloy) the fabricated Ge-Sn layer is expected to be strained. The *in-plane* strain ϵ can be also calculated from the Raman spectra for a given Sn content according to

$$\Delta\omega_{\text{strain}} = a \times x_{\text{Sn}} + b \times \varepsilon, \quad (3)$$

where ϵ is the biaxial strain, $a = -83.11$, $b = -374.53$, and $\Delta\omega_{\text{strain}}$ is the shift of the position of the TO phonon mode with the respect to the relaxed Ge-Sn [30]. The TO phonon mode in GeSnP1 is located at 298.20 cm^{-1}. For 3% Sn in the relaxed Ge-Sn alloy, the peak position of the TO phonon mode in the Raman spectrum should be at 298.01 cm^{-1}. The shift of the peak position of the TO phonon mode in Ge-Sn with 10% Sn is caused by the alloy disorder and increases linearly with the Sn composition. According to Eq. (3), the GeSnP1 layer is compressively strained, with $\epsilon = -0.71\%$. The Raman spectrum obtained from GeSnP3 shows the TO phonon mode at 299.5 cm^{-3}, which indicates the existence of biaxial compressive strain of $\epsilon = -1.06\%$. This is more than 2 times larger than the strain calculated from the XRD data for GeSnP3 ($\epsilon = -0.42\%$). The position of the TO phonon mode in Ge-based alloys depends on the element, strain, and Fano effect [31]. The tensile and compressive strains lead to a shift of the TO phonon mode toward smaller and larger wavenumbers, respectively. The Fano effect in heavily doped *n*-type Ge causes a shift of the TO phonon mode toward smaller wavenumbers. In our case, the shift of the position of the TO phonon mode toward larger wavenumbers with increasing P content in P-doped Ge-Sn alloys can be explained by the change of the phonon energy due to the incorporation of P into Ge-Sn and the generation of compressive strain. Therefore, only the strain calculated from the XRD data is taken into account to analyze the change of the band gap as a function of strain. The calculation of strain from Raman spectra must be done carefully.

C. Band structure

1. Theoretical results

Sn incorporated into Ge modifies not only the lattice parameter but, more importantly, also the band structure of Ge [32,33]. For a particular Sn concentration, it is possible to convert Ge from an indirect-band-gap material to a direct-band-gap material. It was shown that the amount of Sn needed to form a direct band gap in Ge-Sn depends on the strain accumulated in the layer [34]. Therefore, strain engineering will result in a band-gap modification for a Ge-Sn alloy with a fixed Sn concentration. The band gap of Ge-Sn decreases when tensile strain is applied and increases when compressive strain is present. Moreover, it was shown that the band gap of Ge and Ge-Sn alloys decreases with increasing electron concentration due to the band-gap renormalization [1,35]. The band-gap renormalization in relaxed Ge-Sn alloy is on the order of 30 meV

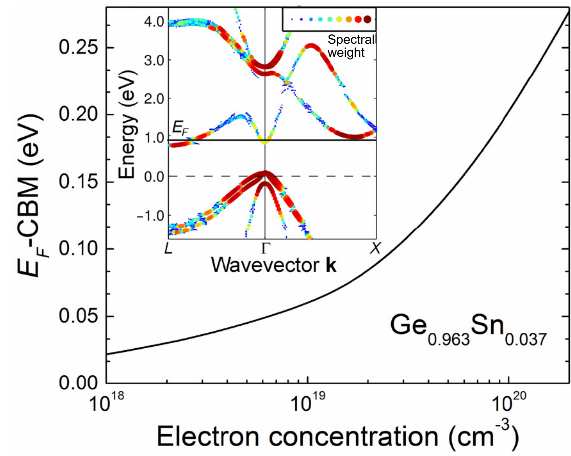

FIG. 5. The calculated relative position of the Fermi energy with respect to the conduction-band minimum in $Ge_{0.963}Sn_{0.037}$ as a function of the doping level. The inset shows an unfolded band diagram of $Ge_{0.963}Sn_{0.037}$, with the horizontal line marking the position of the Fermi energy corresponding to an effective carrier concentration of 1.1×10^{20} cm^{-3}. The color and the size of the points correspond to the spectral weight of the eigenvalues.

at an electron concentration of 2×10^{19} cm^{-3}. At this doping level the Fermi level is still below the bottom of the Γ band, and the Burstein-Moss effect can be ignored. For electron concentrations approaching 10^{20} cm^{-3}, the Ge-Sn alloy becomes strongly degenerate, with the Fermi level located inside the Γ band. Figure 5 shows the relative position of the Fermi energy (E_F) with respect to the conduction-band minimum as a function of electron concentration for fully relaxed Ge-Sn with 3.7% Sn. The inset in Fig. 5 shows the band structure of $Ge_{0.963}$-$Sn_{0.037}$, with the horizontal line marking E_F for an electron concentration of 1.1×10^{20} cm^{-3}. The calculations are performed within density-functional theory with use of the FPLAPW WIEN2k code [36]. A 54-atom supercell ($3 \times 3 \times 3$ multiplication of the primitive diamond unit cell) is used, allowing study of the alloy in intervals of 1.85% Sn. Because of the size of the supercell, the calculation of the band structure for Ge-Sn with 3% Sn was not possible, but the difference of the band gap for 3% Sn and 3.7% Sn is only 20 meV. Within the supercell the Sn atoms are distributed according to special quasirandom structures to approximate a perfect alloy [37]. A full geometry optimization is performed with use of the generalized gradient approximation by Wu and Cohen (GGA-WC) functional [38], and the electronic structure is calculated with use of the Tran-and-Blaha MBJLDA functional [39] to describe the band gap correctly.

The change of the Fermi energy as a function of electron concentration is obtained from the integrated density of states of $Ge_{0.963}Sn_{0.037}$, which is calculated on a dense mesh of $8 \times 8 \times 8$ k points (equivalent to a $24 \times 24 \times 24$

mesh in a primitive unit cell) with use of the modified tetrahedron method [40]. The unfolded band structure in the inset in Fig. 5 is obtained with the spectral-weight approach as implemented in the fold2bloch code [35], where the spectral weight of the eigenvalues is indicated by the color and the size of the points. The simulation data presented do not take into account the band-gap change due to the formation of the P doped Ge-Sn alloy with a reduced lattice parameter. $\Delta E_F = E_F - \text{CBM}$ in $\text{Ge}_{0.963}\text{Sn}_{0.037}$ is deduced to be 210 meV for a doping level of 1.1×10^{20} cm^{-3}. Because of the low density of electron states at the Γ point of the Brillouin zone, E_F is located deep in the conduction band, and the effective absorption edge can be calculated as the energy difference between the valence-band maximum and the E_F position in the conduction band. Koerner *et al*. [41] recently showed that for electron concentrations lower than 5×10^{18} cm^{-3} and Sn concentrations lower than 6%, the band-gap renormalization dominates and the Burstein-Moss effect can be ignored. It was also experimentally verified that the calculated band-gap renormalization is in the range of 20–30 meV for a doping level up to 2×10^{19} cm^{-3} [35].

2. Experimental data

To experimentally verify the band gap in Ge-Sn alloy on doping and strain, the change of the energy of the interband transitions was investigated by spectroscopic ellipsometry. Figure 6(a) shows a plot of $(\alpha h\nu)^2$ versus incident photon energy $(h\nu)$ obtained from nonimplanted and ion-implanted samples followed by FLA. $(\alpha h\nu)^2$ versus $h\nu$ corresponds to the direct-band-gap absorption close to the band-gap edge. The direct band gap of undoped and doped Ge samples was obtained by extrapolation of the fit of the experimental data to the photon-energy axis. The undoped Ge and Ge on Si are relaxed and tensile strained, respectively; therefore, the direct band gap obtained corresponds to the transition between light holes and the Γ valley [42]. The (Ge,Sn)P alloys are compressively strained, indicating that the extrapolated band gap is associated with the transition between heavy holes and the Γ valley.

The inset in Fig. 6(a) shows the low- and high-energy parts of the second derivative of the imaginary part of the dielectric function in the vicinity of the E_0, E_1, and $E_1 + \Delta_1$ critical points obtained from bulk Ge, tensile-strained virgin Ge-on-Si and P-doped Ge-Sn. The numerically obtained second derivatives are smoothed with use of Savitzky-Golay coefficients. The critical point E_1 in GeSnP1 is redshifted by 20 meV in comparison with that in virgin Ge. The critical point E_1 in GeSnP2 and GeSnP3 shifts back to the original position of the virgin Ge with increasing P concentration. The critical points E_1 and $E_1 + \Delta_1$ should not be affected by the Burstein-Moss effect. The observed redshift is because band-gap renormalization occurs [43]. The E_0 critical point in Ge-Sn alloys is significantly redshifted in comparison with bulk Ge. In general, the redshift of E_0 with increasing P concentration is expected, which indicates band-gap narrowing in heavily doped *n*-type Ge-Sn similarly to what happens in highly doped *n*-type Ge [44,45]. However, the occurrence of the Burstein-Moss effect cannot be fully ignored for heavily doped Ge-Sn layers. According to Hall-effect measurements, the room-temperature effective electron concentration in P-doped samples is 7.2×10^{19} cm^{-3} for GeSnP1 and 10.5×10^{19} cm^{-3} for GeSnP3. The mean carrier concentrations for a particular doping level are estimated with use of the measured sheet Hall concentration and the thickness of the doped layer deduced from SIMS measurements. The room-temperature electron mobility increases from 140 cm^2/Vs in GeSnP1 to 175 cm^2/Vs in GeSnP3. Since the Sn concentration is the same in all samples, the enhancement of the carrier mobility and the change of the band gap can be associated with

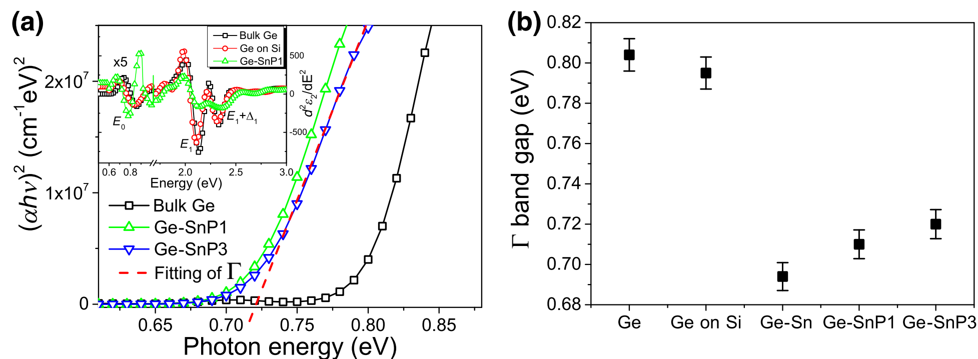

FIG. 6. Plot of $(\alpha h\nu)^2$ as a function of photon energy obtained from spectroscopic ellipsometry measurements (a) and the energy of the Γ band gap (b) in intrinsic bulk Ge, undoped tensile-strained Ge on Si, undoped relaxed Ge-Sn, and heavily-P-doped Ge-Sn with 3% Sn extracted from (a) by linear fitting of $(\alpha h\nu)^2$ versus $h\nu$. The inset in (a) shows the second derivative of the imaginary part of the dielectric function $[d^2\epsilon_2(E)/dE^2]$ as obtained by spectroscopic ellipsometry from bulk Ge, nonimplanted tensile-strained Ge on Si, and GeSnP1.

the strain engineering and the band-gap renormalization, respectively [46,47].

Figure 6(b) shows the values for the direct-band-gap Γ in bulk Ge, tensile-stained Ge on Si, undoped Ge-Sn, and very-heavily-doped Ge-Sn alloys. The final band gap of the fabricated heavily doped (Ge,Sn)P alloys is the result of the band-gap renormalization, strain, and Burstein-Moss effect. In undoped Ge-Sn with 3% Sn and compressive strain $\epsilon = -0.42\%$, $E_g(\Gamma)$ is around 0.75 eV. For the band-gap renormalization at an electron concentration of 10.5×10^{19} cm^{-3} for GeSnP3, the band gap should decrease by $\Delta E = 110$ meV to $E_g(\Gamma) = 0.64$ eV. However, the measured direct band gap in GeSnP3 is $E_g(\Gamma) = 0.72$ eV, which is 80 meV bigger than expected. The increase of the band gap in P-doped Ge-Sn alloy with increasing effective carrier concentration above 7×10^{19} cm^{-3} must be caused by the Burstein-Moss effect due to ultrahigh *n*-type doping [48]. Therefore, in contrast to intrinsic or lightly doped *n*-type Ge-Sn, in strongly degenerate *n*-type Ge-Sn a blueshift of the effective absorption edge is expected. This means that even strain-free Ge-Sn with Sn content on the order of 3% and E_F located deep in the direct band gap may become a quasi-direct band gap semiconductor (see the inset in Fig. 5).

IV. CONCLUSIONS

Highly-P-doped n^{++}-type Ge-Sn-on-Si alloys are fabricated by ion-beam implantation and postimplantation nonequilibrium thermal processing. Effective-strain and Fermi-energy engineering are achieved by P codoping and RFLA. The compensation of biaxial compressive strain and the lattice-parameter reduction results in a band-gap change accompanied by an enhancement of the carrier mobility. Both the reduction of the lattice parameter and the Burstein-Moss effect are proven to be responsible for the blueshift of the absorption edge and partial compensation of the band-gap renormalization in P-doped Ge-Sn alloys. The whole fabrication procedure is fully compatible with CMOS technology, which paves the way for Ge-based optoelectronics.

ACKNOWLEDGMENTS

Support by the Ion Beam Center at Helmholtz-Zentrum Dresden-Rossendorf is gratefully acknowledged. We thank Andrea Scholz for XRD measurements and Romy Aniol for TEM specimen preparation. This work was partially supported by the German Academic Exchange Service (DAAD; project ID 57216326) and the National Science Centre, Poland, under Grant No. 2016/23/B/ST7/03451. Y.B. thanks the Alexander von Humboldt Foundation for a postdoctoral fellowship. The funding of the Talos transmission electron microscope by the German Federal Ministry of Education of Research (BMBF), Grant No. 03SF0451, in the framework of Helmholtz Energy Materials Characterization Platform (HEMCP) is gratefully acknowledged.

[1] R. Camacho-Aguilera, Z. Han, Y. Cai, L. C. Kimerling, and J. Michel, Direct band gap narrowing in highly doped Ge, Appl. Phys. Lett. **102**, 152106 (2013).

[2] S. Zaima, O. Nakatsuka, N. Taoka, M. Kurosawa, W. Takeuchi, and M. Sakashita, Growth and applications of GeSn-related group-IV semiconductor materials, Sci. Technol. Adv. Mater. **16**, 043502 (2015).

[3] S. Saito, A. Z. Al-Attili, K. Oda, and Y. Ishikawa, Towards monolithic integration of germanium light sources on silicon chips, Semicond. Sci. Technol. **31**, 043002 (2016).

[4] J. Liu, L. C. Kimerling, and J. Michel, Monolithic Ge-on-Si lasers for large-scale electronic–photonic integration, Semicond. Sci. Technol. **27**, 094006 (2012).

[5] J. Liu, X. Sun, D. Pan, X. Wang, L. C. Kimerling, T. L. Koch, and J. Michel, Tensile-strained, n-type Ge as a gain medium for monolithic laser integration on Si, Opt. Express **15**, 11272 (2007).

[6] M. El Kurdi, G. Fishman, S. Sauvage, and P. Boucauda, Band structure and optical gain of tensile-strained germanium based on a 30 band k·p formalism, J. Appl. Phys. **107**, 013710 (2010).

[7] Y. Bai, K. E. Lee, C. Cheng, M. L. Lee, and E. A. Fitzgerald, Photoluminescence and secondary ion mass spectrometry investigation of unintentional doping in epitaxial germanium thin films grown on III-V compound by metal-organic chemical vapor deposition, J. Appl. Phys. **104**, 084518 (2008).

[8] D. Stange, S. Wirths, N. von den Driesch, G. Muer, T. Stoica, Z. Ikonic, J. M. Hartmann, S. Mantl, D. Grützmacher, and D. Buca, Optical Transitions in Direct-Bandgap $Ge_{1-x}Sn_x$ Alloys, ACS Photonics **2**, 1539 (2015).

[9] S. Wirths, R. Geiger, N. von den Driesch, G. Mussler, T. Stoica, S. Mantl, Z. Ikonic, M. Luysberg, S. Chiussi, J. M. Hartmann, H. Sigg, J. Faist, D. Buca, and D. Grützmacher, Lasing in direct-bandgap GeSn alloy grown on Si, Nat. Photonics **9**, 88 (2015).

[10] S. Prucnal, F. Liu, M. Voelskow, L. Vines, L. Rebohle, D. Lang, Y. Berencén, S. Andric, R. Boettger, M. Helm, S. Zhou, and W. Skorupa, Ultra-doped n-type germanium thin films for sensing in the mid-infrared, Sci. Rep. **6**, 27643 (2016).

[11] S. Prucnal, L. Rebohle, and W. Skorupa, Doping by flash lamp annealing, Mater. Sci. Semicond. Process. **62**, 115 (2017).

[12] L. Rebohle, S. Prucnal, and W. Skorupa, A review of thermal processing in the subsecond range: semiconductors and beyond, Semicond. Sci. Technol. **31**, 103001 (2016).

[13] W. Skorupa, T. Schumann, and L. Rebohle, Millisecond thermal processing using flash lamps for the advancement of thin layers and functional coatings, Surf. Coat. Technol. **314**, 169 (2017).

[14] E. Simoen, M. Schaekers, J. Liu, J. Luo, C. Zhao, K. Barla, and N. Collaert, Defect engineering for shallow n-type

junctions in germanium: Facts and fiction, Phys. Status Solidi A **213**, 2799 (2016).

[15] J. von Borany, R. Grötzschel, K.-H. Heinig, A. Markwitz, B. Schmidt, W. Skorupa, and H.-J. Thees, The formation of narrow nanocluster bands in Ge-implanted SiO_2-layers, Solid-State Electron. **43**, 1159 (1999).

[16] C. Wündisch, M. Posselt, B. Schmidt, V. Heera, T. Schumann, A. Mücklich, R. Grötzschel, W. Skorupa, T. Clarysse, E. Simoen, and H. Hortenbach, Millisecond flash lamp annealing of shallow implanted layers in Ge, Appl. Phys. Lett. **95**, 252107 (2009).

[17] S. Prucnal, F. Liu, Y. Berencén, L. Vines, L. Bischoff, J. Grenzer, S. Andric, S. Tiagulskyi, K. Pyszniak, M. Turek, A. Drozdziel, M. Helm, S. Zhou, and W. Skorupa, Enhancement of carrier mobility in thin Ge layer by Sn co-doping, Semicond. Sci. Technol. **31**, 105012 (2016).

[18] T. Janssens, C. Huyghebaert, D. Vanhaeren, G. Winderickx, A. Satta, M. Meuris, and W. Vandervorst, Heavy ion implantation in Ge: Dramatic radiation induced morphology in Ge, J. Vac. Sci. Technol. B **24**, 510 (2006).

[19] R. Böttger, A. Keller, L. Bischoff, and S. Facsko, Mapping the local elastic properties of nanostructured germanium surfaces: from nanoporous sponges to self-organized nanodots, Nanotechnology **24**, 115702 (2013).

[20] D. V. Likhachev, Selecting the right number of knots for B-spline parameterization of the dielectric functions in spectroscopic ellipsometry data analysis, Thin Solid Films **636**, 519 (2017).

[21] J. F. Ziegler, SRIM-2003, Nucl. Instrum. Methods Phys. Res. B **219-220**, 1027 (2004).

[22] L. Nikolova, et al., Nanocrystallization of amorphous germanium films observed with nanosecond temporal resolution, Appl. Phys. Lett. **97**, 203102 (2010).

[23] M. Wittmer, C-Y Ting, I. Ohdomari, and K. N. Tu, Redistribution of As during Pd2Si formation: Ion channeling measurements, J. Appl. Phys. **53**, 6781 (1982).

[24] S. Zhou, et al., Hyperdoping silicon with selenium: solid vs. liquid phase epitaxy, Sci. Rep. **5**, 8329 (2015).

[25] A. Claverie, S. Koffel, N. Cherkashin, G. Benassayag, and P. Scheiblin, Amorphization, recrystallization and end of range defects in germanium, Thin Solid Films **518**, 2307 (2010).

[26] H. Ye and J. Yu, Germanium epitaxy on silicon, Sci. Technol. Adv. Mater. **15**, 024601 (2014).

[27] N. Bhargava, M. Coppinger, J. P. Gupta, L. Wielunski, and J. Kolodzey, Lattice constant and substitutional composition of GeSn alloys grown by molecular beam epitaxy, Appl. Phys. Lett. **103**, 041908 (2013).

[28] C. Xu, C. L. Senaratne, J. Kouvetakis, and J. Menendez, Experimental doping dependence of the lattice parameter in n-type Ge: Identifying the correct theoretical framework by comparison with Si, Phys. Rev. B **93**, 041201 (2016).

[29] Y. Yamamoto, P. Zaumseil, T. Arguirov, M. Kittler, and B. Tillack, Low threading dislocation density Ge deposited on Si (1 0 0) using RPCVD, Solid-State Electron. **60**, 2 (2011).

[30] R. Cheng, W. Wang, X. Gong, L. Sun, P. Guo, H. Hu, Z. Shen, G. Han, and Y.-C. Yeo, Relaxed and strained patterned germanium-tin structures: A Raman scattering study, ECS J. Solid State Sci. Technol. **2**, P138 (2013).

[31] N. Fukata, K. Sato, M. Mitome, Y. Bando, T. Sekiguchi, M. Kirkham, J-il. Hong, Z. L. Wang, and R. L. Snyder, Doping and Raman characterization of boron and phosphorus atoms in germanium nanowires, ACS Nano **4**, 3807 (2010).

[32] K. Gao, S. Prucnal, R. Huebner, C. Baehtz, I. Skorupa, Y. Wang, W. Skorupa, M. Helm, and S. Zhou, $Ge_{1-x}Sn_x$ alloys synthesized by ion implantation and pulsed laser melting, Appl. Phys. Lett. **105**, 042107 (2014).

[33] S. Wirths, D. Stange, M.-A. Pampillón, A. T. Tiedemann, G. Mussler, A. Fox, U. Breuer, B. Baert, E. San Andrés, N. D. Nguyen, J.-M. Hartmann, Z. Ikonic, S. Mantl, and Dan Buca, High-k gate stacks on low bandgap tensile strained Ge and GeSn alloys for field-effect transistors, ACS Appl. Mater. Interfaces **7**, 62 (2015).

[34] A. Gassenq, L. Milord, J. Aubin, K. Guilloy, S. Tardif, N. Pauc, J. Rothman, A. Chelnokov, J. M. Hartmann, V. Reboud, and V. Calvo, Gamma bandgap determination in pseudomorphic GeSn layers grown on Ge with up to 15% Sn content, Appl. Phys. Lett. **109**, 242107 (2016).

[35] L. Jiang, J. D. Gallagher, C. L. Senaratne, T. Aoki, J. Mathews, J. Kouvetakis, and J. Menéndez, Compositional dependence of the direct and indirect band gaps in $Ge_{1-y}Sn_y$ alloys from room temperature photoluminescence: implications for the indirect to direct gap crossover in intrinsic and n-type materials, Semicond. Sci. Technol. **29**, 115028 (2014).

[36] J. Perdew, K. Burke, and M. Ernzerhof, Generalized Gradient Approximation Made Simple, Phys. Rev. Lett. **77**, 3865 (1996).

[37] A. van de Walle, P. Tiwary, M. de Jong, D. L. Olmsted, M. Asta, A. Dick, D. Shin, Y. Wang, L. Q. Chen, and Z. K. Liu, Efficient stochastic generation of special quasirandom structures, Calphad **42**, 13 (2013).

[38] F. Tran and P. Blaha, Accurate Band Gaps of Semiconductors and Insulators with a Semilocal Exchange-Correlation Potential, Phys. Rev. Lett. **102**, 226401 (2009).

[39] O. Rubel, A. Bokhanchuk, S. Ahmed, and E. Assmann, Unfolding the band structure of disordered solids: From bound states to high-mobility Kane fermions, Phys. Rev. B **90**, 115202 (2014).

[40] P. E. Blöchl, O. Jepsen, and O. K. Andersen, Improved tetrahedron method for Brillouin-zone integrations, Phys. Rev. B **49**, 16223 (1994).

[41] R. Koerner, I. A. Fischer, D. Schwarz, C. Clausen, M. Oehme, and J. Schulze, MBE grown germanium tunnel-junctions—Burstein-Moss effect and band-edge luminescence in the Ge Zener-Emitter, Semicond. Sci. Technol. **32**, 124005 (2017).

[42] H. Tran, W. Du, S. A. Ghetmiri, A. Mosleh, G. Sun, R. A. Soref, J. Margetis, J. Tolle, B. Li, H. A. Naseem, and S.-Q. Yu, Systematic study of $Ge_{1-x}Sn_x$ absorption coefficient and refractive index for the device applications of Si-based optoelectronics, J. Appl. Phys. **119**, 103106 (2016).

[43] C. Xu, N. S. Fernando, S. Zollner, J. Kouvetakis, and J. Menéndez, Observation of Phase-Filling Singularities in the Optical Dielectric Function of Highly Doped n-Type Ge, Phys. Rev. Lett. **118**, 267402 (2017).

[44] L. Baldassarre, E. Sakat, J. Frigerio, A. Samarelli, K. Gallacher, E. Calandrini, G. Isella, D. J. Paul, M. Ortolani, and P. Biagioni, Midinfrared plasmon-enhanced spectroscopy

with germanium antennas on silicon substrates, Nano Lett. **15**, 7225 (2015).

[45] S. Prucnal, Y. Berencén, M. Wang, L. Rebohle, R. Böttger, I. A. Fischer, L. Augel, M. Oehme, J. Schulze, M. Voelskow, M. Helm, W. Skorupa, and S. Zhou, Ex-situ n+ doping of GeSn alloys via non-equilibrium processing, Semicond. Sci. Technol. **33**, 065008 (2018).

[46] F. Dybała, K. Żelazna, H. Maczko, M. Gladysiewicz, J. Misiewicz, R. Kudrawiec, H. Lin, R. Chen, C. Shang, Y. Huo, T. I. Kamins, and J. S. Harris, Electromodulation spectroscopy of direct optical transitions in $Ge_{1-x}Sn_x$ layers under hydrostatic pressure and built-in strain, J. Appl. Phys. **119**, 215703 (2016).

[47] M. P. Polak, P. Scharoch, and R. Kudrawiec, The electronic band structure of $Ge_{1-x}Sn_x$ in the full composition range: indirect, direct, and inverted gaps regimes, band offsets, and the Burstein–Moss effect, J. Phys. D: Appl. Phys **50**, 195103 (2017).

[48] P. Blaha, K. Schwarz, G. K. H. Madsen, D. Kvasnicka, and J. Luitz, *WIEN2k, An Augmented Plane Wave + Local Orbitals Program for Calculating Crystal Properties* (Karlheinz Schwarz, Techn. Universitat Wien, Austria, 2001)